Silicon Nanowire Based Angle Robust Ultrasensitive Hyperbolic Metamaterial Biosensor: Electronic Supplementary Information

1. SUGGESTED FABRICATION

It is vital to consider the realistic fabrication technique and tolerances when designing our proposed NW-based HMM structure. Initially, the fabrication of the proposed n-Si nanowire biosensor begins with preparing a glass substrate coated with PMMA (Polymethyl methacrylate) using sputtering [1]. Additionally, we can grow n-doped silicon by the vapor–liquid–solid (VLS) mechanism [2]. After that, a thin layer of n-doped silicon (n-Si) is deposited onto the PMMA surface. We can fabricate a Si nanowire pattern using electron beam lithography and electroplating methods [3, 4]. These methods enable precise control over nanowire geometry, with diameter and spacing variations usually within ∼5% [5], and doping concentrations kept within ∼5–10% [6]. These variations are acceptable for the proposed design because minor changes mainly shift the resonance wavelength, which can be adjusted during calibration. We can soften the PMMA photoresist layers by exposing our proposed structure to ultraviolet (UV) light. Finally, we can use acetone to lift off the PMMA layer from the structure [7]. In addition to fabrication, we can also address integration challenges. Silane-based linkers can be used for covalent attachment between silicon nanowires and biomolecules in sensor functionalization [8]. We can control uniform analyte transport using some methods, such as soft lithography and microchannel integration for fluid handling [9]. Moreover, device packaging is an important factor to ensure stable performance and protection from environmental degradation. Hence, some techniques, such as advanced encapsulation and chip-level integration, can be conducive for biosensor packaging [10]. The proposed fabrication technique for our HMM model is depicted in Fig. S1.

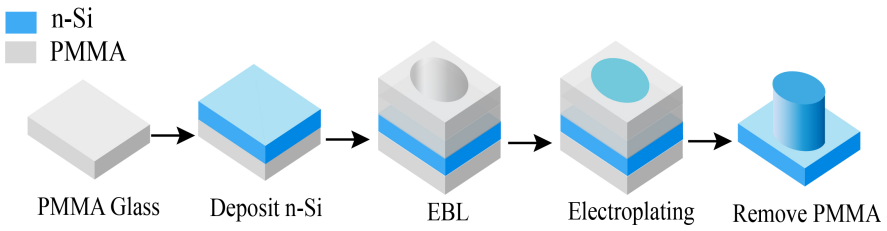

Fig. S1. Schematic illustration of suggested fabrication technique for our proposed n-Si NW biosensor structure.

2. BULK N-SI PERMITTIVITY

We obtained the complex permittivity of the n-Si using the Drude model, which is defined by,

$$\epsilon_c = \epsilon' + i\epsilon'' \tag{S1}$$

where ϵ' and ϵ'' are the real and imaginary parts of the relative permittivity that govern the polarization and polarization-driven loss of the n-Si. We calculated the effective permittivity ϵ', ϵ'' for different doping concentrations, as illustrated in Fig. S2.

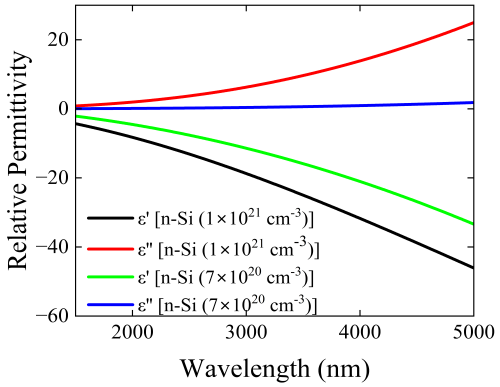

Fig. S2. Relative permittivity real (ϵ') and imaginary (ϵ'') parts of n-Si for different doping concentration.

3. REFRACTIVE INDEX OF NS1 PROTEIN:

The RI of NS1 protein was estimated from the molar refraction of its chemical constituents, primarily amino acid residues forming peptide chains [11]. Since proteins contain approximately 20 standard amino acid residues, each with diverse functional groups that influence molar refraction, we considered the average molar refraction for the NS1 protein. We calculated the average molar refraction $[R]$ of the NS1 protein using the refraction of different chemical bonds and compounds in the protein. The corresponding molar refraction of primary amino acids was considered from [12] and the average molar refraction, specific volume, and molar mass were obtained as 26.726, 0.74 cc, and 120 g, respectively. The refractive index was obtained by,

$$[R] = \frac{(n^2-1)}{(n^2+2)}\frac{M}{\rho}. \tag{S2}$$

Here, $[R]$, M, ρ, and n are the molar refraction, molar mass, density, and the refractive index of the NS1 protein, respectively. The refractive index was determined to be 1.5.

4. IMPACT OF DOPING CONCENTRATION

Our proposed biosensor structure was based on n-Si NW and n-Si base. However, there were two types of n-Si doping. We investigated the effect of doping concentration of NW and base based on reflection spectra, as shown in Figs. S3(a) and (b). We obtained the best doping concentration of n-Si for Nw was 1×10^{21} cm^{-3}. On the other hand, we observed the minimum reflection peak and FWHM when the base doping concentration was 7×10^{20} cm^{-3}.

5. LIGHT CONFINEMENT ANALYSIS

The total phase experienced by a single round trip into the n-Si NW by a photon is expressed by,

$$\phi_{total} = \phi_{pro} + \phi_{NW-air} + \phi_{NW-base}. \tag{S3}$$

Here, ϕ_{pro}, ϕ_{NW-air}, and $\phi_{NW-base}$ are the propagation phase and nontrivial phase shifts at the top and bottom interfaces of the NW, defined as

$$\phi_{NW-base} = \arg\left(\frac{\eta_{\mathrm{HMM}}/\cos\theta_i - \eta}{\eta_{\mathrm{HMM}}/\cos\theta_i + \eta}\right), \tag{S4}$$

$$\phi_{NW-air} = \arg\left(\frac{\eta_{\mathrm{HMM}}/\cos\theta_i - \eta_o}{\eta_{\mathrm{HMM}}/\cos\theta_i + \eta_o}\right), \text{and} \tag{S5}$$

$$\phi_{\mathrm{pro}} = \mathrm{Re}(2\delta_{\mathrm{HMM}}). \tag{S6}$$

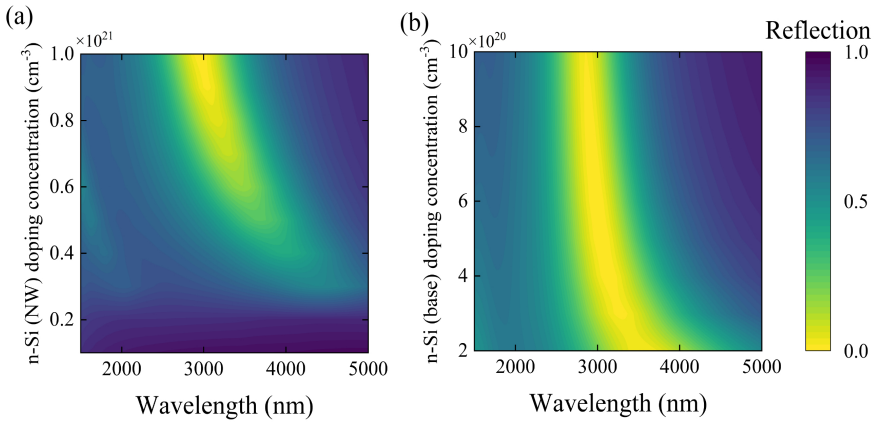

Fig. S3. Illustration of reflection spectra varying the doping concentration of n-Si (a) NW and (b) base.

The electric field relation at the interface is given by

$$\begin{bmatrix} \frac{E_b}{E_c} \\ \frac{H_b}{E_c} \end{bmatrix} = \begin{bmatrix} \cos\delta_b & \frac{i\sin\delta_b}{\eta_b} \\ i\eta_b \sin\delta_b & \cos\delta_b \end{bmatrix} \begin{bmatrix} 1 \\ \eta_o \end{bmatrix}, \text{and} \tag{S7}$$

$$\eta = \frac{H_a}{E_a}. \tag{S8}$$

Here, η_{HMM} and η are the admittance of the HMM structure and the admittance seen by forward propagating light at the bottom of the HMM structure, which accounts for the nontrivial reflection phase shift. We considered the propagation phase shift ϕ_{pro} for a round trip.

6. PERFECT ADMITTANCE MATCHING

We investigated the admittance of the HMM biosensor structure using the formula defined as

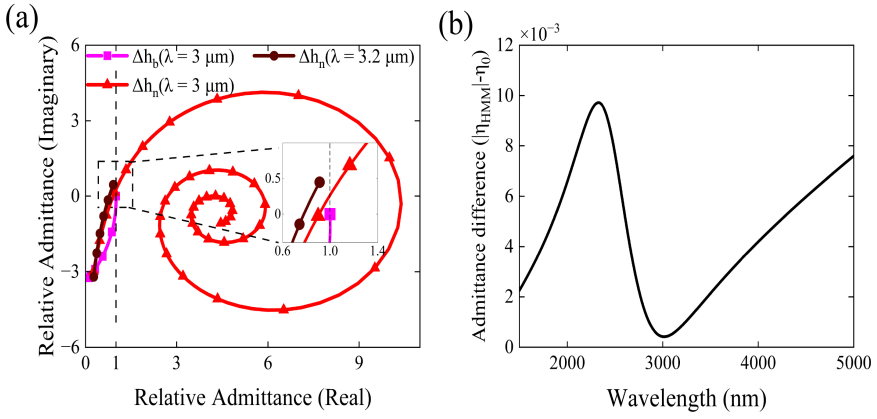

Fig. S4. (a) Illustration of relative admittance at resonant wavelength ($3\mu m$) of the HMM biosensor structure for h_b and h_n and relative admittance at wavelength ($3.2\mu m$) for h_n. (b) The admittance difference between the vacuum and our proposed nanowire HMM structure.

$$Y_k = \frac{i\eta_{\mathrm{HMM}}\sin(\delta_{\mathrm{HMM}}) + \cos(\delta_{\mathrm{HMM}})Y_b}{\cos(\delta_{\mathrm{HMM}}) + \frac{i\sin(\delta_{\mathrm{HMM}})}{\eta_{\mathrm{HMM}}}Y_b} \tag{S9}$$

Figure S4 (a) shows that the relative admittance seen by the resonant wave is unity. As we introduced an optically thin n-Si base h_b layer, the relative admittance follows the path away from unity indicated by the magenta arrow. At 200 nm n-Si base, the relative admittance was about $-3i$.

Moreover, when we introduced an optically thin HMM layer, the relative admittance traverses through a spiral path. The spiral path meets a unity relative admittance point at an 80 nm thin HMM layer. Thus, a perfect zero reflection is achieved at an 80 nm thin HMM over a 200 nm thin n-Si base layer at the resonance wavelength (3000 nm).

The increase in h_n took the relative admittance over unity, followed by the spiral path (red). Thus, the reflection at the resonant wavelength increased for h_n over 80 nm. Moreover, the relative admittance path for 3.2 μm wavelength is shown in the black curve. The relative admittance for a 100 nm thin HMM layer approached unity (indicated by the point). Hence, a resonance shift in reflectance to a larger wavelength is observed under the change in h_n. Moreover, the relative admittance difference of the structure is shown in Fig. S4 (b). The admittance difference showed a perfect match at 2999 nm wavelength, which enhances electric field confinement between the nanowires.

7. PLASMA CHARGE

We investigated the plasmonic resonance on the HMM biosensor structure by employing the Maxwell divergence formula defined as,

$$\nabla \cdot E = \rho. \tag{S10}$$

Where E and ρ are the electric field intensity and charge density at the HMM biosensor, respectively. We obtained E using FDTD simulation and subsequently calculated the charge density using S10, We assumed that the bond charge at the surface is negligible and the plasmons are

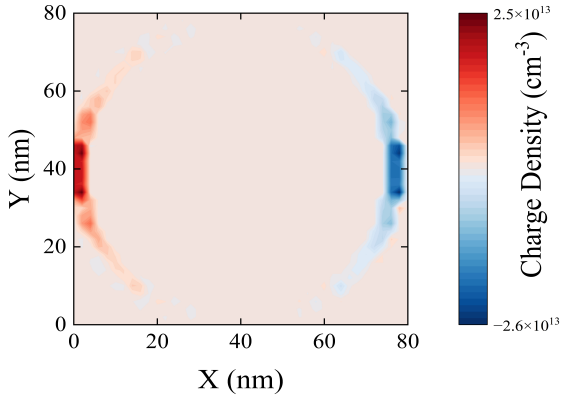

Fig. S5. Illustration of charge density profile of NW for our proposed biosensor structure in X-Y view.

illustrated in Fig. S5. The results illustrated that the enhanced localized surface plasmons confine E between subsequent NWs.

8. MASS SENSITIVITY

We calculated the mass sensitivity by observing the maximum resonance wavelength shift $\Delta\lambda$ due to the presence of a single NS1 protein molecule. We obtained a maximum $\Delta\lambda$ of 14 nm caused by the presence of a 90×10^{-21} cc NS1 protein.

The average density of a protein is calculated in Section S3 as 1 g/0.74 cc, and the corresponding mass of a single NS1 protein is 1.215×10^{-4} fg (73 kDa).

The mass sensitivity based on the resonance shift of the reflection spectra of our HMM biosensor structure is calculated as

$$\frac{14\,\text{nm}}{73\,\text{kDa}} = 0.192\ \text{nm/kDa}.$$

9. RESPONSE FOR DIFFERENT BIOMOLECULES

We analyzed our biosensor structure response behavior for detecting 28% hemoglobin and 50% glucose, as shown in Fig. S6. We changed the surrounding RI of the NW for injecting hemoglobin and glucose. All other parameters remained constant. We adopted the RI of 28% Hemoglobin of 1.3598 [13]. Moreover, we used the RI of 50% glucose of 1.38 [14]. We observed a visible shift in wavelength in the reflection spectra for these biomarkers. Thus, we inferred that our proposed structure can be used for the detection of other biomarkers.

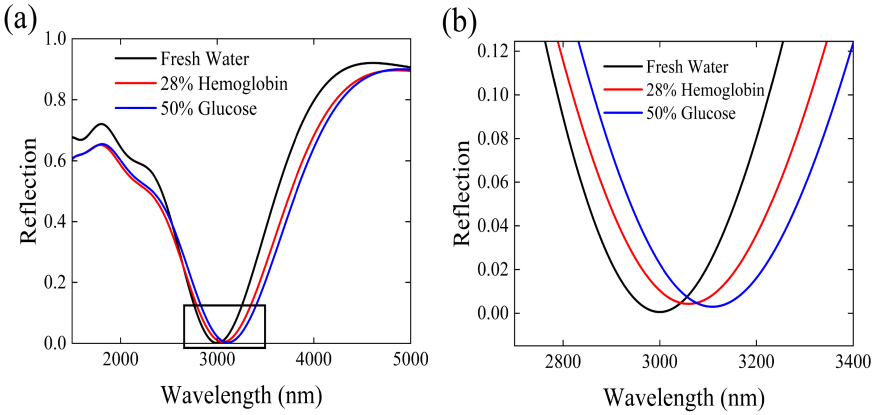

Fig. S6. Illustration and (b) zoom view of reflection spectra with injecting different biomolecules (Hemoglobin, Glucose) into fresh water on our proposed HMM structure.

REFERENCES

1. R. Hurley and H. Gamble, "Thin film sputtered silicon for silicon wafer bonding applications," Vacuum **70**, 131–140 (2003).
2. D. Sharma, A. Motayed, S. Krylyuk, *et al.*, "Detection of deep-levels in doped silicon nanowires using low-frequency noise spectroscopy," IEEE transactions on electron devices **60**, 4206–4212 (2013).
3. S. H. Baek, S. Lee, J.-H. Bae, *et al.*, "Nanopillar and nanohole fabrication via mixed lithography," Mater. Res. Express **7**, 035008 (2020).
4. S. Kilian, K. McCarthy, K. Stokes, *et al.*, "Direct growth of si, ge, and si–ge heterostructure nanowires using electroplated zn: An inexpensive seeding technique for li-ion alloying anodes," Small **17**, 2005443 (2021).
5. J. San Nah, S. C. Barman, M. A. Zahed, *et al.*, "A wearable microfluidics-integrated impedimetric immunosensor based on ti3c2tx mxene incorporated laser-burned graphene for noninvasive sweat cortisol detection," Sensors Actuators B: Chem. **329**, 129206 (2021).
6. Y. Cui, X. Duan, J. Hu, and C. M. Lieber, "Doping and electrical transport in silicon nanowires," The journal physical chemistry B **104**, 5213–5216 (2000).
7. B. Zhuang, S. Li, S. Li, and J. Yin, "Ways to eliminate pmma residues on graphene—superclean graphene," Carbon **173**, 609–636 (2021).
8. F. Patolsky, G. Zheng, and C. M. Lieber, "Fabrication of silicon nanowire devices for ultrasensitive, label-free, real-time detection of biological and chemical species," Nat. protocols **1**, 1711–1724 (2006).
9. G. M. Whitesides, "The origins and the future of microfluidics," nature **442**, 368–373 (2006).
10. Y. Zheng, G. Zhao, Y. Zhang, and R. Gao, "On-chip loading and unloading of cryoprotectants facilitate cell cryopreservation by rapid freezing," Sensors Actuators B: Chem. **255**, 647–656 (2018).
11. K.-T. Lee, S. Seo, J. Y. Lee, and L. J. Guo, "Strong resonance effect in a lossy medium-based optical cavity for angle robust spectrum filters," Adv. Mater. (2014).
12. T. L. McMeekin, M. L. Groves, and N. J. Hipp, "Refractive indices of amino acids, proteins, and related substances," (1964).

13. E. N. Lazareva and V. V. Tuchin, "Measurement of refractive index of hemoglobin in the visible/nir spectral range," J. biomedical optics **23**, 035004–035004 (2018).
14. K. E. You, N. Uddin, T. H. Kim, *et al.*, "Highly sensitive detection of biological substances using microfluidic enhanced fabry-perot etalon-based optical biosensors," Sensors Actuators B: Chem. **277**, 62–68 (2018).